Open access • Journal Article • DOI:10.1103/PHYSREVE.66.021301

Calculation of the incremental stress-strain relation of a polygonal packing.

Fernando Alonso-Marroquin, Hans J. Herrmann

Institutions: University of Stuttgart

Published on: 01 Aug 2002 - Physical Review E (American Physical Society)

Topics: Plasticity, Constitutive equation, Deformation (engineering), Stress–strain curve and Quasistatic process

Calculation of the incremental stress-strain relation of a polygonal packing

F. Alonso-Marroquin and H. J. Herrmann
ICA1, University of Stuttgart, Pfaffenwaldring 27, 70569 Stuttgart, Germany
(Received 25 March 2002; published 20 August 2002)

The constitutive relation of the quasistatic deformation on two-dimensional packed samples of polygons is calculated using molecular dynamics simulations. The stress values at which the system remains stable are bounded by a failure surface, which shows a power law dependence on the pressure. Below the failure surface, nonlinear elasticity and plastic deformation are obtained, which are evaluated in the framework of the incremental linear theory. The results show that the stiffness tensor can be directly related to the microcontact rearrangements. The plasticity obeys a nonassociated flow rule with a plastic limit surface that does not agree with the failure surface.

DOI: 10.1103/PhysRevE.66.021301 PACS number(s): 45.70.Cc, 83.10.Gr, 61.43.Bn, 83.80.Nb

I. INTRODUCTION

The nonlinear and irreversible behavior of soils has been described by different constitutive theories [1,2]. Here the stress-strain relation is postulated using a certain number of material parameters which are measured in experimental tests. These continuous theories have been used for many geotechnical applications. Excavations, foundations, and landslides are some few examples of these applications.

Recently, the investigation of soils at the grain scale has become possible using numerical simulations [3]. They evidence that the stress is transmitted through a heterogeneous network of interparticle contacts [4]. The geometric change of this network during deformation reveals a structural anisotropy induced by shearing [5]. Although these results provide valuable insights into the behavior of soils, few issues are given to derive the continuous relations from the discrete models.

In this paper the stress-strain relation of a two-dimensional discrete model is calculated explicitly using numerical simulations. An internal variable is included in this continuous relation, which is related to the anisotropy of the contact network. The results show that it is possible to characterize the mechanical behavior of soils at the macroscopic scale using particle models. In effect, we demonstrate that simple mechanical laws at the grain level are able to reproduce the complex behavior of the deformation of soils.

Usually, disks or spheres are used in the modeling of granular materials. The simplicity of their geometry allows one to reduce the computer time of calculations, but they do not take into account the diversity of the shapes of the grains in the realistic materials. A more detailed description is presented here by using randomly generated convex polygons. As presented by Tillemans and Herrmann [6], the interaction between the polygons could be handled by letting the polygons interpenetrate each other and calculating the force as a function of their overlap. This approach has been successfully applied to model different processes, such as fragmentation [7,8], damage [9], strain localization, and earthquakes [6].

This paper is organized as follows. A suitable contact force law is introduced in Sec. II A, which attempts to combine the Hertz contact law with the Coulomb friction criterion. The boundary condition is introduced in Sec. II B by a flexible membrane that surrounds the sample. The modeling with such a membrane is very advantageous since it allows one to implement a stress-controlled loading without any restriction in the deformation of the boundary. The strain response is calculated in Sec. III for different stress increments applied on identically generated samples. The results are discussed in Sec. IV in the framework of the theory of elastoplasticity.

II. MODEL

The polygons of this model are generated using a simple version of the Voronoi tessellation: First, we set a random point in each cell of a regular square lattice, then each polygon is constructed assigning to each point that part of the plane that is nearer to it than to any other point. Each polygon is subjected to interparticle contact forces and boundary forces. They are inserted in Newton's equation of motion as we explain below.

A. Contact force

Usually, the interaction between two solid bodies in contact is described by a force applied on the flattened contact surface between them. Given two polygons in contact, such surface is obtained from the geometrical construction shown in Fig. 1. The points C_1 and C_2 result from the intersection between the edges of the polygons. The contact surface is taken as the segment that lies between those points. The vector $\vec{S}=\overrightarrow{C_1C_2}$ defines an intrinsic coordinate system at the contact $(\hat{t},\hat{n})$, where $\hat{t}=\vec{S}/|\vec{S}|$ and $\hat{n}$ is perpendicular to it. The deformation length is given by $\delta=a/|\vec{S}|$, where a is the overlap area between the polygons. $\vec{\ell}$ is the branch vector, which connects the center of mass of the polygon to the point of application of the contact force, which is supposed to be the center of mass of the overlap area.

The normal elastic force is taken proportional to the deformation length as $f_n^e=k_n\delta$; the tangential force is calculated from the simplified Coulomb friction law with a single friction coefficient $\mu_s=\mu_d=\mu$. Here μ_s is the static and μ_d the dynamic friction coefficient. This tangential force is

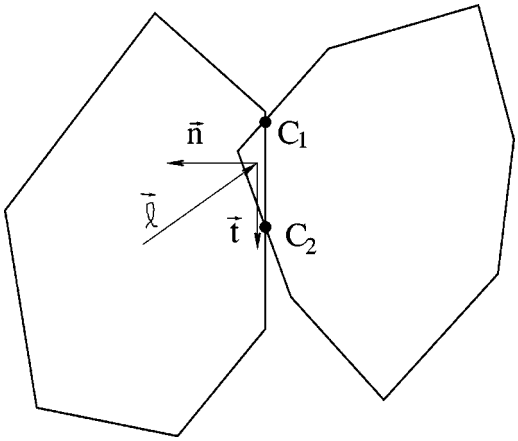

FIG. 1. Contact surface as defined from the geometry of overlap.

implemented by an elastic spring $f_t^e = -k_t \xi$, where ξ grows linearly with the tangential displacement of the contact, whenever $|f_t^e| < \mu f_n^e$. We used the straightforward calculation of ξ proposed by Brendel [10],

$$\xi(t) = \int_0^t v_t(t') \Theta(|f_t^e(t')| - \mu f_n^e(t')) dt', \tag{1}$$

where Θ is the Heaviside function and $\vec{v}$ is the relative velocity at the contact, which depends on the linear velocity $\vec{v}_i$ and angular velocity $\vec{\omega}_i$ of the particles in contact according to

$$\vec{v} = \vec{v}_i - \vec{v}_j - \vec{\omega}_i \times \vec{\ell}_i . + \vec{\omega}_j \times \vec{\ell}_j . \tag{2}$$

B. Boundary forces

Let us now discuss how to apply the stress on the sample. One way to do that would be to apply a perpendicular force on each edge of the polygons belonging to the external contour of the sample. Actually, this does not work because this force will act on all the fjords of the boundary. It produces an uncontrollable growth of cracks that with time ends up destroying the sample. Thus, it is necessary to introduce a flexible membrane in order to restrict the boundary points that are subjected to the external stress.

The algorithm to identify the boundary is rather simple. The lowest vertex p from all the polygons of the sample is chosen as the first point of the boundary list b_1. In Fig. 2 P is the polygon that contains p, and $q \in P \cap Q$ is the first intersection point between the polygons P and Q in counterclockwise orientation with respect to p. Starting from p, the vertices of P in counterclockwise orientation are included in the boundary list until q is reached. Next, q is included in the boundary list. Then, the vertices of Q between q and the next intersection point $r \in Q \cap R$ in the counterclockwise orientation are included into the list. The same procedure is applied until one reaches the lowest vertex p again. This is a very fast algorithm, because it only makes use of the contact points between the polygons, which are previously calculated to obtain the contact force.

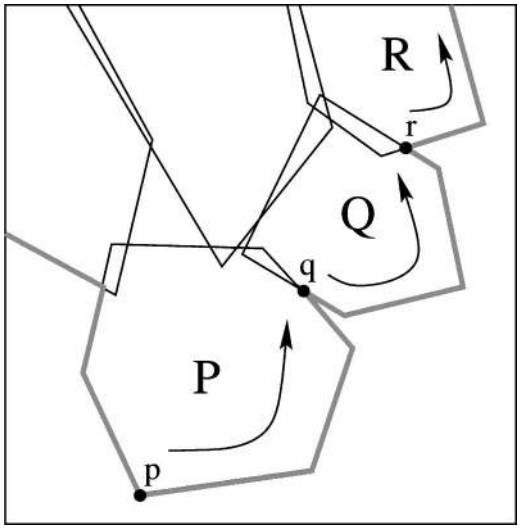

FIG. 2. Algorithm used to find the boundary.

The set of points that are in contact with the membrane are selected using a recursive algorithm. It is initialized with the vertices of the smallest convex polygon that encloses the boundary (see Fig. 3). The lowest point of the boundary is selected as the first vertex of the polygon $m_1 = b_1$. The second one m_2 is the boundary point b_i that minimizes the angle $\angle(\overrightarrow{b_1 b_i})$ with respect to the horizontal. The third one m_3 is the boundary point b_i such that the angle $\angle(\overrightarrow{m_2 b_i}, \overrightarrow{m_1 m_2})$ is minimal. The algorithm is recursively applied until the lowest vertex m_1 is reached again.

The points of the boundary are iteratively included in the list m_i using the bending criterion proposed by Åström *et al.* [11]: For each pair of consecutive vertices of the membrane $m_i = b_i$ and $m_{i+1} = b_j$ we choose that point from the subset $\{b_k\}_{i \leq k \leq j}$ that maximizes the bending angle $\theta_b = \angle(\overrightarrow{b_k b_i}, \overrightarrow{b_k b_j})$. This point is included into the list, whenever $\theta_b \geq \theta_{th}$. Here θ_{th} is a threshold angle for bending. This algorithm is repeatedly applied until there are no more points satisfying the bending condition.

The final result gives a set of segments $\{\overrightarrow{m_i m_{i+1}}\}$ lying on the boundary of the sample. In order to apply the boundary forces, those segments are divided into two groups: *A*-type segments are those that coincide with an edge of a boundary polygon; *B*-type segments connect the vertices of two different boundary polygons.

On each segment of the membrane $\overrightarrow{m_i m_{i+1}}$ a force $f_i = \sigma_i N_i$ is applied, where σ_i is the local stress and N_i is the 90° counterclockwise rotation of $\overrightarrow{m_i m_{i+1}}$. This force is transmitted to the polygons in contact with it: if the segment is of *A* type, this force is applied in its midpoint; if the segment is of *B* type, half of the force is applied at each one of the vertices connected by this segment.

C. Molecular dynamics simulation

Before we implement the numerical solution of Newton's equations it is convenient to make a dimensional analysis of

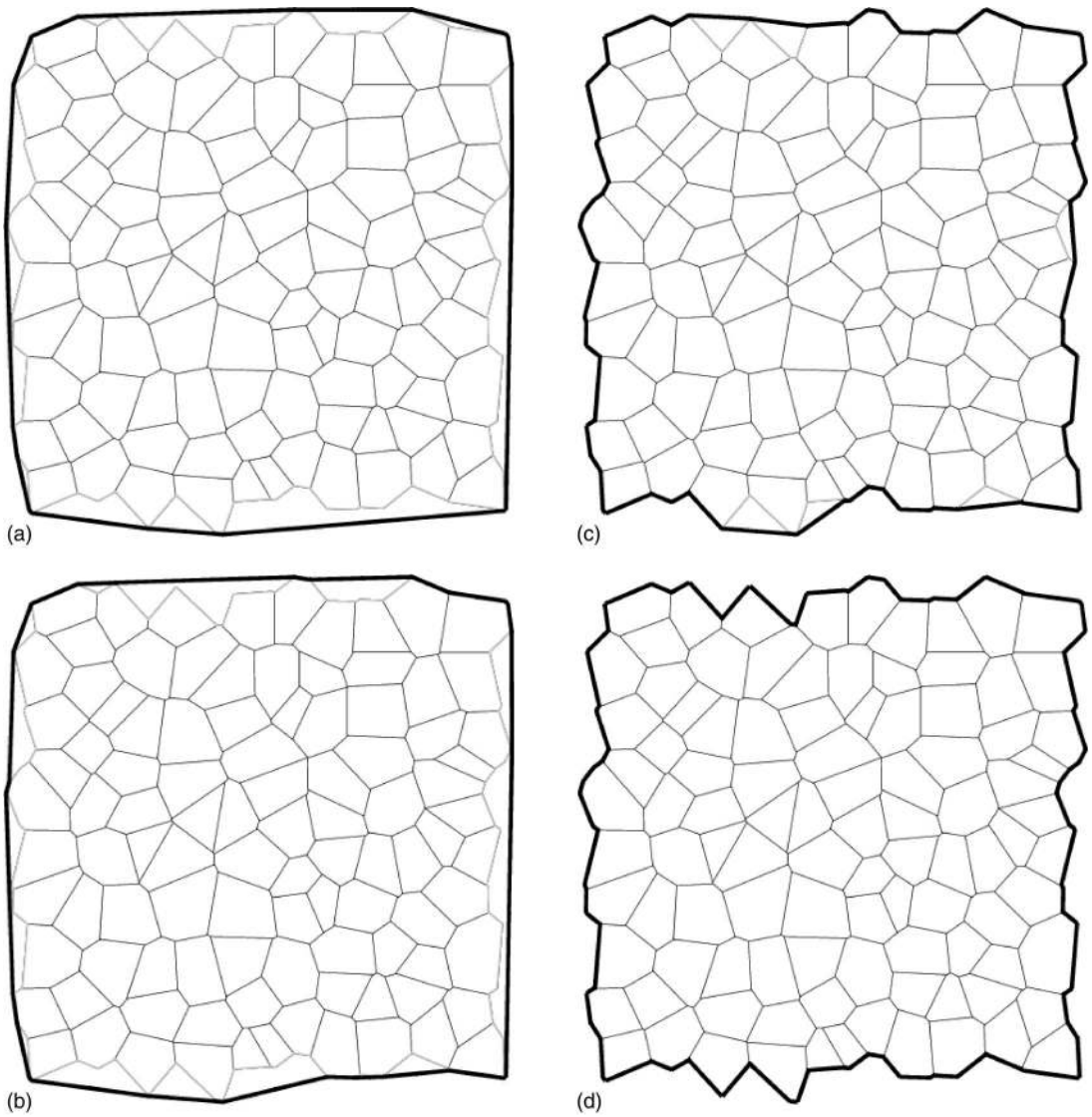

FIG. 3. Membrane obtained with threshold bending angle $\theta_{th}=\pi$, $3\pi/4$, $\pi/2$, and $\pi/4$. The first one corresponds to the minimum convex polygon that encloses the sample.

the parameters. In such way we can keep the scale invariance of the model and reduce the parameters to a minimum of dimensionless constants. All the polygons are supposed to have the same density. The mass m_i of each polygon is measured in units of the mean mass m_0 of the Voronoi tessellation. The time is measured in fractions of the total loading time t_0. The evolution of the position $\vec{x}_i$ and the orientation φ_i of the i_{th} polygon is governed by the equations of motion,

$$\lambda^2 m_i \ddot{\vec{x}}_i + \sum_c \vec{f}_i^c + \sum_{c_b} \frac{\sigma_i^b}{k_n} \vec{f}_i^b = \vec{0},$$

$$\lambda^2 I_i \ddot{\varphi}_i + \sum_c \vec{\ell}_i^c \times \vec{f}_i^c + \sum_{c_b} \frac{\sigma_i^b}{k_n} \vec{\ell}_i^b \times \vec{f}_i^b = \vec{0}. \tag{3}$$

The sums go over all those particles and boundary segments that are in contact with the i_{th} polygon. The interparticle contact forces $\vec{f}_i^c$ and boundary forces $\vec{f}_i^b$ are given by

$$\vec{f}_i^c = (\delta_i^c + \lambda\gamma m v_n^c)\hat{n}_i^c + \zeta(\xi_i^c - \lambda\gamma m v_t^c)\hat{t}_i^c,$$

$$\vec{f}_i^b = \vec{N}_i^b - \lambda\gamma m_i \vec{v}_i. \tag{4}$$

Here δ_i^c and ξ_i^c denote the deformation length and the tangential displacement of the contact, which were defined in Sec. II A; σ_i^b is the stress applied on the boundary segment T_i^b, defined in Sec. II B. Artificial viscous terms must be included in Eq. (4) to keep the stability of the numerical solution and reduce the acoustic waves generated during the loading process. $\vec{v}^c$ denotes the relative velocity at the contact [Eq. (2)] and $m=(1/m_i+1/m_j)^{-1}$ the effective mass of the two polygons in contact.

There are four microscopic parameters in the model: the viscosity γ, the ratio $\lambda=t_s/t_o$ between the characteristic period of oscillation $t_s=\sqrt{k_n/m_0}$ and the loading time t_0, the friction coefficient μ, and the ratio $\zeta=k_t/k_n$ between the tangential k_t and normal k_n stiffness of the interparticle con-

TABLE I. Dimensionless variables.

Variable	Ratio	Default value
Viscosity	γ	0.1
Friction coefficient	μ	0.25
Time ratio	$\lambda = t_s/t_o$	8.0×10^{-4}
Stiffness ratio	$\zeta = k_t/k_n$	0.33
Granularity	ℓ_0/H_0	0.1
Shape ratio	W_0/H_0	1.0
Bending angle	θ_{th}	0.25π

tacts. The viscosity factor γ is related to the normal restitution coefficient [12]. It was taken large enough to have a high dissipation, but not too large to keep the numerical stability of the method. The ratio λ was chosen small enough in order to avoid rate dependence in the strain response, corresponding to the quasistatic approximation. Technically, it is done by looking for the value of λ such that a reduction of it by half makes a change of the strain response less than 5%.

The two parameters ζ and μ determine the constitutive response of the system. For example, the micromechanical analysis of the strain response shows that the Young's modulus and Poisson's ratio depend on ζ [13]. On the other hand, μ can be directly related to the friction angle of the material [14]. Although the study of the dependence of the constitutive response on those parameters is an important point, such quantities have been kept fixed in this work.

The boundary conditions yield more dimensional parameters. The initial height H_0 and width W_0 of the sample, and the characteristic length ℓ_0 of the polygons define two geometrical parameters, which are the shape ratio W_0/H_0 and the granularity ℓ_0/H_0 of the sample (see Table I).

In order to keep overlaps much smaller than the characteristic area of the polygons, the ratio σ_i/k_n between the stress applied on the membrane and the stiffness of the contacts is restricted to small values. This was implemented by fixing the contact stiffness to a value close to the experimental granular stiffness $k_n = 160$ MPa. Then the stress is chosen in such a way that it does not exceed 1% of this value.

III. STRESS-STRAIN CALCULATION

A. Theoretical background

The macroscopic state of the system is characterized by the stress tensor and the void ratio e. The area fraction of voids in the sample defines the void ratio. Initially $e_0 = 0$ due to the Voronoi tessellation used. The stress controlled test was restricted to stress states without off-diagonal components. The diagonal components, the axial δ_1 and lateral δ_3 stress, define the stress vector,

$$\tilde{\sigma} = \begin{bmatrix} p \\ q \end{bmatrix} = \frac{1}{2}\begin{bmatrix} \delta_1 + \delta_3 \\ \delta_1 - \delta_3 \end{bmatrix}, \tag{5}$$

where p and q are the pressure and the shear stress. The domain of admissible stresses is bounded by the failure surface. When the system reaches this surface it becomes unstable and fails.

TABLE II. Principal modes of loading according to the orientation of $\hat{\theta}$.

0°	Isotropic compression	$dp>0$	$dq=0$
45°	Axial loading	$d\sigma_1>0$	$d\sigma_3=0$
90°	Pure shear	$dp=0$	$dq>0$
135°	Lateral loading	$d\sigma_1=0$	$d\sigma_3>0$
180°	Isotropic expansion	$dp<0$	$dq=0$
225°	Axial stretching	$d\sigma_1<0$	$d\sigma_3=0$
270°	Pure shear	$dp=0$	$dq<0$
315°	Lateral stretching	$d\sigma_1=0$	$d\sigma_3<0$

Before failure, the constitutive behavior can be obtained performing small changes in the stress and evaluating the resultant deformation. An infinitesimal change of the stress vector $d\tilde{\sigma}$ produces an infinitesimal deformation of the sample, which is given by a change of height dH and width dW. This defines the axial strain $d\epsilon_1 = dH/H$ and lateral strain $d\epsilon_3 = dW/W$ increments. The volumetric strain $d\epsilon_v$ and the shear strain $d\epsilon_\gamma$ increments define the incremental strain vector,

$$d\tilde{\epsilon} = \begin{bmatrix} d\epsilon_v \\ d\epsilon_\gamma \end{bmatrix} = \begin{bmatrix} d\epsilon_1 + d\epsilon_3 \\ d\epsilon_1 - d\epsilon_3 \end{bmatrix}. \tag{6}$$

Each state of the sample is related to a single point in the stress space, and the quasistatic evolution of the system is represented by the movement of this point in the stress space. The constitutive relation is formulated taking the incremental strain as a function of the incremental stress and the stress state

$$d\tilde{\epsilon} = \mathcal{F}(d\tilde{\sigma}, \tilde{\sigma}). \tag{7}$$

If there is no rate dependence in the constitutive equation, $\mathcal{F}(d\tilde{\sigma})$ is an homogeneous function of degree 1. In this case, the application of the Euler identity [15] shows that Eq. (7) can be reduced to

$$d\tilde{\epsilon} = M(\hat{\theta}, \tilde{\sigma}) d\tilde{\sigma}. \tag{8}$$

Where $\hat{\theta}$ is the unitary vector defining a specific direction in the stress space,

$$\hat{\theta} = \frac{d\tilde{\sigma}}{|d\tilde{\sigma}|} \equiv \begin{bmatrix} \cos\theta \\ \sin\theta \end{bmatrix}, \quad |d\tilde{\sigma}| = \sqrt{dp^2 + dq^2}. \tag{9}$$

The constitutive relation results from the calculation of $d\tilde{\epsilon}(\theta)$, where each value of θ is related to a particular mode of loading. Some special modes are listed in Table II.

The relation (8) has been proposed by Darve [15] and it contains all the possible constitutive equations. In order to interpret our particular results, it is convenient to make some approximations: First, if the load increments are taken small enough, the tensor $M(\theta)$ can be supposed to be linear in

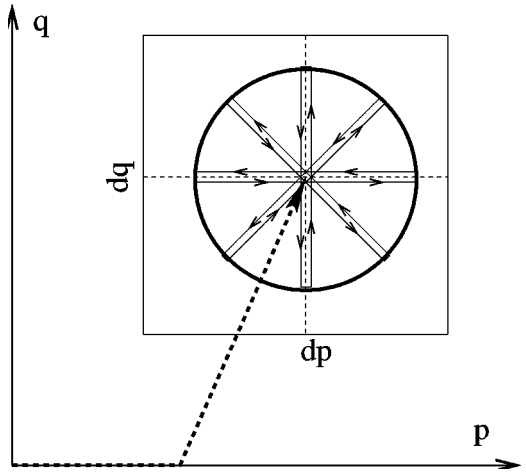

FIG. 4. Procedure to obtain the constitutive behavior: (1) The sample is driven to the stress state $\tilde{\sigma}$, with pressure p and shear stress q. (2) It is loaded from $\tilde{\sigma}$ to $\tilde{\sigma}+d\tilde{\sigma}$. (3) It is unloaded to the original stress state $\tilde{\sigma}$.

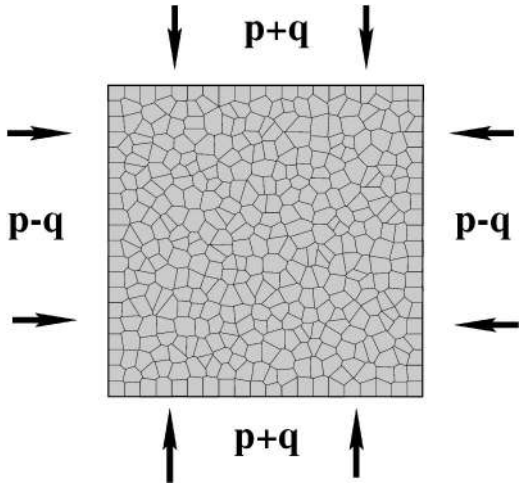

FIG. 5. Axial stress $\sigma_1=p+q$ and lateral stress $\sigma_3=p-q$ in a stress controlled test. They are applied on the boundary of the tessellated sample of polygons.

each stress direction. Then, we assume that the strain can be separated in an elastic (recoverable) and a plastic (unrecoverable) component,

$$d\tilde{\epsilon}=d\tilde{\epsilon}^e+d\tilde{\epsilon}^p, \tag{10}$$

$$d\tilde{\epsilon}^e=D(\tilde{\sigma})d\tilde{\sigma}, \tag{11}$$

$$d\tilde{\epsilon}^p=J(\theta,\tilde{\sigma})d\tilde{\sigma}. \tag{12}$$

Here, D^{-1} defines the stiffness tensor, and $J=M-D$ the flow rule of plasticity, which results from the calculation of $d\tilde{\epsilon}^e(\theta)$ and $d\tilde{\epsilon}^p(\theta)$.

B. The method

The numerical method presented here was proposed by Bardet [16]. It allows one to find the elastic $d\tilde{\epsilon}^e$ and plastic $d\tilde{\epsilon}^p$ components of the strain as functions of the stress state $\tilde{\sigma}$ and the stress direction θ. Figure 4 shows the three steps of the procedure.

(1) The sample is driven to the stress state $\tilde{\sigma}$. First, it is isotropically compressed until it reaches the stress value $\delta_1=\delta_3=p-q$. Next, it is subjected to axial loading, in order to increase the axial stress δ_1 to $p+q$ (see Fig. 5). When the stress state $\tilde{\sigma}=[pq]^T$ is reached, (A^T being the transpose of A) the sample is allowed to relax.

(2) Loading the sample from $\tilde{\sigma}$ to $\tilde{\sigma}+d\tilde{\sigma}$ the strain increment $d\tilde{\epsilon}$ is obtained. This procedure is implemented choosing different stress directions according to Eq. (9). Here the stress modulus is fixed to $|d\tilde{\sigma}|=10^{-4}p$.

(3) The sample is unloaded until the original stress state $\tilde{\sigma}$ is reached. Then one finds a remaining strain $d\tilde{\epsilon}^p$ that corresponds to the plastic component of the incremental strain. Since the stress increments are taken small enough, the unloaded stress-strain path is practically elastic. Thus, the difference $d\tilde{\epsilon}^e=d\tilde{\epsilon}-d\tilde{\epsilon}^p$ represents the elastic component of the strain.

One could be concerned about the dependence of the strain response on the way how the stress state is reached. We found that there is not remarkable dependence of the strain response on the stress path, whenever the stress components are quasistatic and monotonically increased. Otherwise, a strong reduction in the plastic component of the strain is observed. In fact, when the plastic response is calculated after the sample is unloaded, the plasticity is smaller than that one calculated after a monotonic load. Furthermore, there is no plastic component in the strain response when elastic waves are previously generated in the sample. Those memory effects suggest that the plastic component of the strain depends on the history of the deformation, and is kept unchanged only if the sample is subjected to quasistatic and monotonic loading.

Figure 6 shows the load-unload paths and the corresponding strain response. They were taken from a stress state with $q=0.5p$. The end of the load paths in the stress space map into a strain envelope response $d\tilde{\epsilon}(\theta)$ in the strain space. Likewise, the end of the unload paths map into a plastic envelope response $d\tilde{\epsilon}^p(\theta)$. The yield direction ϕ can be found from this response, as the direction in the stress space where the plastic response is maximal. The flow rule can be obtained taking the direction ψ of the maximal plastic response in the strain space. These angles do not agree, which reveals the necessity to analyze this behavior in the framework of the nonassociated theory of plasticity (see Sec. IV C).

IV. CONSTITUTIVE RELATION

Figure 7 summarizes the global elastoplastic behavior. The elastic response, calculated from Eq. (10), has a centered ellipse as envelope response. This can be related to the microcontact structure using a local linear relation in each point of the stress space (see Sec. IV B). The solid line represents

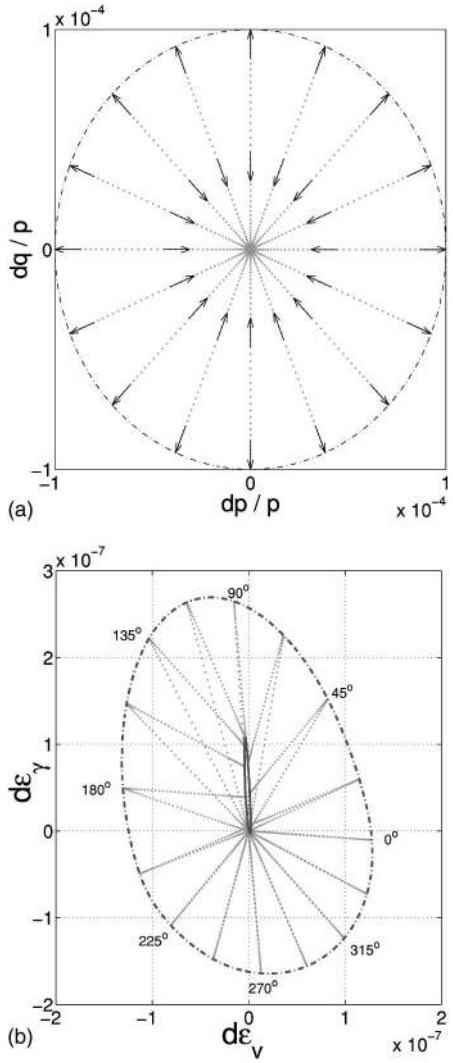

FIG. 6. Stress-strain relation resulting from the load-unload test. Dotted lines represent the paths in the stress and strain spaces. The dash-dotted line gives the strain envelope response and the solid line is the plastic envelope response.

the failure surface that separates the stable states from the unstable ones (see Sec. IV A). The plastic envelope response is almost on a straight line. The modulus and the orientation of this envelope depend on the stress state through a certain number of material parameters, which are given in Sec. IV C. All the quantities obtained in this section have been calculated from the average over five different samples of 10×10 particles each one.

A. Failure surface

The failure line was calculated looking for the values of stress for which the system becomes unstable: for each pressure p, there is a critical shear stress $q_c(p)$, below which the sample reaches a stable state with an exponential decay of its kinetic energy. For shear stress values above the critical one, the sample develops an instability and fails. Figure 8 shows the interface between these two stress states, which can be accurately fitted by the power law

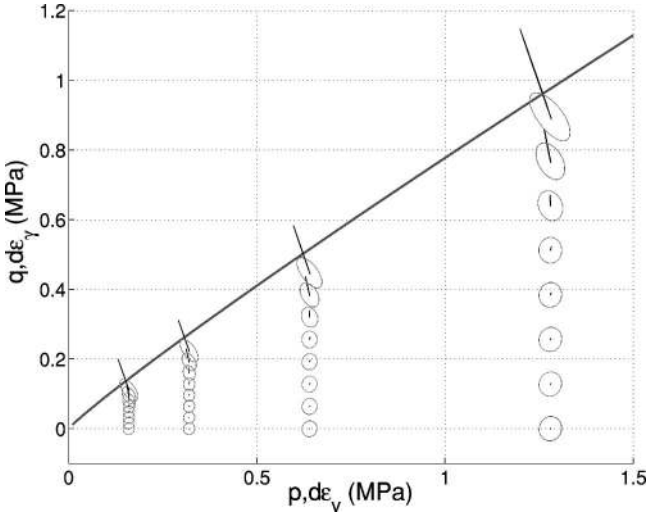

FIG. 7. Elastic response $d\tilde{\epsilon}^e$ and plastic response $d\tilde{\epsilon}^p$ resulting from the application of different loading modes with $|d\tilde{\sigma}|=10^{-4}p$. The solid line represents the failure surface.

$$\frac{q_c}{p_0}=\mu^*\left(\frac{p}{p_0}\right)^{\beta}. \tag{13}$$

Here $p_0=1.0$ MPa is the reference pressure, and $\mu^*=0.78\pm 0.03$ is the Mohr-Coulomb friction coefficient [1]. The power law dependence on the pressure, with exponent $\beta=0.92\pm 0.02$, implies a significant deviation from the Mohr-Coulomb theory. Moreover, the empirical criteria of failure for most rocks [17] shows a power law dependence of the form of Eq. (13). It seems that additional features beyond the Mohr-Coulomb analysis are taking place when the sample fails, which will be discussed in Sec. IV C.

B. Stiffness

Hooke's law of elasticity states that the stiffness tensor of isotropic materials can be written in terms of two material

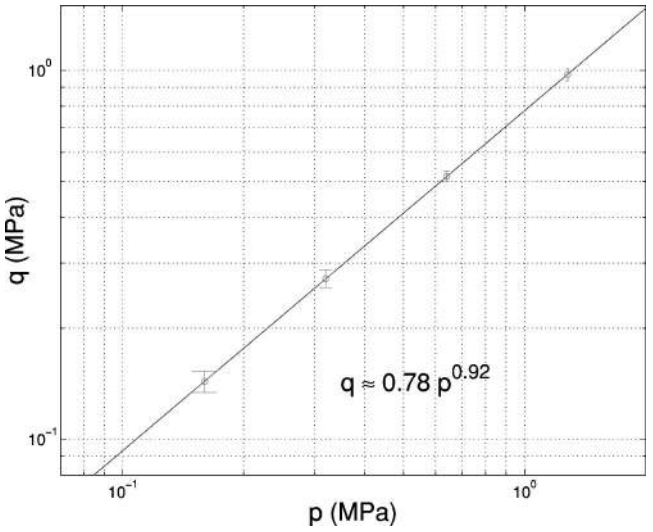

FIG. 8. Failure surface. The continuous line represents the power law fit.

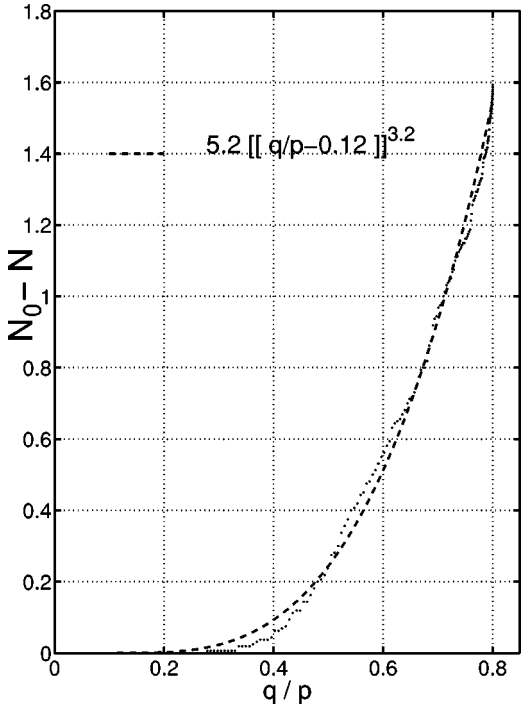

FIG. 9. Reduction of the mean coordination number of contacts (dotted line). The data have been fitted to a truncated power law (dashed line). See Eq. (29).

parameters, i.e., Young's modulus E and Poisson's ratio ν. However, the isotropy is not fulfilled when the stress state is far from the hydrostatic axis. Indeed, numerical simulations [5,18] and photoelastic experiments [19] on granular materials show that the loading induces a significant deviation from isotropy in the contact network.

The anisotropy of the granular sample can be characterized by the distribution of the microcontact normal vectors $\hat{n}_i^c$ (see Fig. 1). Our numerical simulations show that the structural changes of microcontacts are principally due to the opening of contacts whose normal vectors are nearly aligned around the direction perpendicular to the load. Let us call $N(\varphi)\Delta\varphi$ the number of contacts per particle oriented between the angles φ and $\varphi+\Delta\varphi$, measured with respect to the direction along which the sample is loaded. The lowest order of anisotropy can be described by the expression

$$N(\varphi)=\frac{1}{2\pi}[N+(N_0-N)\cos(2\varphi)]. \tag{14}$$

Here N is the average coordination number of the polygons, whose initial value $N_0=6.0$ reduces as the load is increased. Figure 9 shows this reduction. A critical line is found around $q=0.12p$, below which there are no structural changes in the contact network. Above this limit an induced anisotropy arises due to opened contacts whose amount follows a power law dependence.

In order to describe the effect of the anisotropy in the elastic response we proceed as follows: first, an additional parameter α is included in Hooke's law

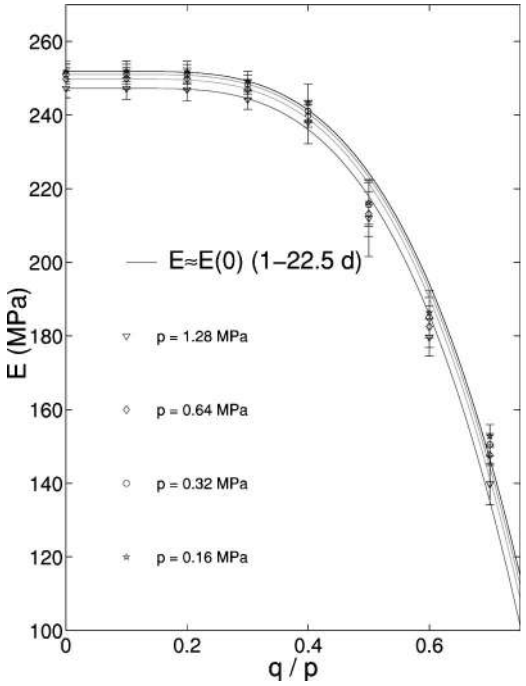

FIG. 10. Young's modulus. The solid line is the linear approximation of $E(d)$. See Eq. (24).

$$\begin{bmatrix} d\epsilon_1^e \\ d\epsilon_3^e \end{bmatrix}=\frac{1}{E}\begin{bmatrix} 1-\alpha & -\nu \\ -\nu & 1+\alpha \end{bmatrix}\begin{bmatrix} d\sigma_1 \\ d\sigma_3 \end{bmatrix}. \tag{15}$$

Then, these three parameters are supposed to be dependent on the internal damage parameter d,

$$d=\frac{N_0-N}{N_0}. \tag{16}$$

The tensor D defined in Eq. (11) is calculated from Eq. (15) using the definition of the stress and strain vectors given in Eqs. (5) and (6). One obtains

$$D=\frac{2}{E}\begin{bmatrix} 1-\nu & -\alpha \\ -\alpha & 1+\nu \end{bmatrix}. \tag{17}$$

The diagonal components of this tensor are the inverse of the bulk modulus and of the shear modulus, respectively. The nondiagonal component results from the anisotropy of the sample, and it couples the compression mode with the shearing deformation. These three variables are calculated from the elastic response $d\tilde{\epsilon}^e(\theta)$ by the introduction of the following function:

$$R(\theta)=\frac{d\tilde{\sigma}^T d\tilde{\epsilon}^e}{|d\tilde{\sigma}|^2}. \tag{18}$$

Substituting Eqs. (11) and (9) into Eq. (18), one sees that R is the quadratic form of D,

$$R(\theta)=\hat{\theta}^T D\,\hat{\theta}=\frac{2}{E}[1-\nu\cos(2\theta)-\alpha\sin(2\theta)]. \tag{19}$$

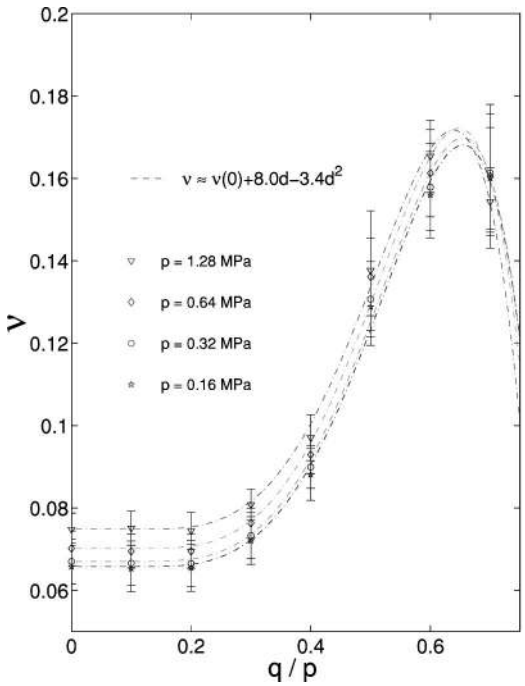

FIG. 11. Poisson's ratio. The dashed line is the quadratic approximation of $\nu(d)$. See Eq. (24).

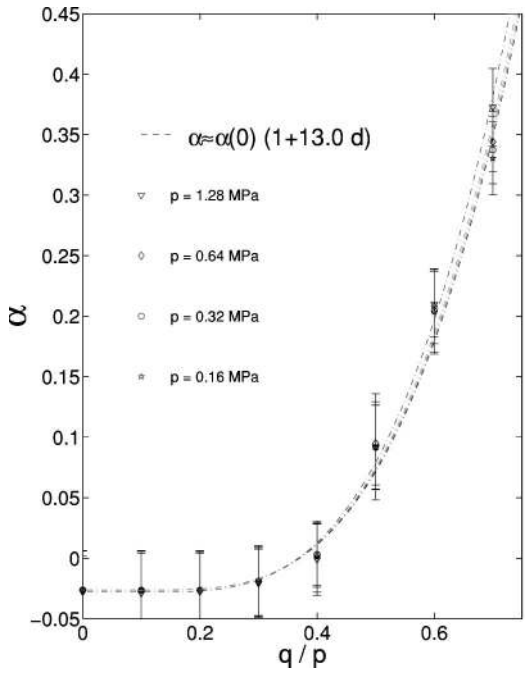

FIG. 12. Anisotropy parameter. The dashed line is the linear approximation of $\alpha(d)$. See Eq. (24).

Using this equation, the components of D can be evaluated as the Fourier coefficients of R,

$$\frac{1}{E}=\frac{1}{4\pi}\int_0^{2\pi}R(\theta)d\theta, \tag{20}$$

$$\nu=-\frac{E}{2\pi}\int_0^{2\pi}R(\theta)\cos(2\theta)d\theta, \tag{21}$$

$$\alpha=-\frac{E}{2\pi}\int_0^{2\pi}R(\theta)\sin(2\theta)d\theta. \tag{22}$$

Figures 10, 11, and 12 show the results of the calculation of Young's modulus E, Poisson's ratio ν, and the anisotropy factor α, respectively. Below the limit of isotropy, Hooke's law can be applied: $E\approx E_0$, $\nu\approx\nu_0$ and $\alpha\approx 0$. On the other hand, above the limit of isotropy a reduction of Young's modulus is found, along with an increase of Poisson's ratio and the anisotropy factor. The functional dependence of those parameters on the internal damage parameter d is evaluated developing their Taylor's series around $d=0$,

$$\begin{aligned}E(d)&=E(0)+E'(0)d+O(d^2),\\ \alpha(d)&=\alpha(0)+\alpha'(0)d+O(d^2),\\ \nu(d)&=\nu(0)+\nu'(0)d+\nu''(0)d^2+O(d^3).\end{aligned} \tag{23}$$

The coefficients of this expansion are calculated from the best fitting of those expansions. Figures 10 and 12 show that the linear approximation is good enough to reproduce Young's modulus and the anisotropy factor. The fit of Poisson's ratio, however, requires the inclusion of a quadratic approximation, implying that it has a nonlinear dependence on the damage parameter (Fig. 11).

C. Plastic flow

The formulation of the nonassociated theory of plasticity requires the evaluation of three material functions, i.e., the yield direction ϕ, the flow direction ψ, and the plastic modulus h. These quantities can be calculated from the plastic response $d\tilde{\epsilon}^p(\theta)$, as follows.

The yield direction is given by the incremental stress direction ϕ with maximal plastic response

$$|d\tilde{\epsilon}^p(\phi)|=\max_\theta|d\tilde{\epsilon}^p(\theta)|. \tag{24}$$

The flow direction is defined from the orientation of the plastic response at its maximum value

$$\psi=\arctan\left(\frac{d\epsilon_\gamma^p}{d\epsilon_v^p}\right)\Bigg|_{\theta=\phi}. \tag{25}$$

The plastic modulus is obtained from the modulus of the maximal plastic response

$$\frac{1}{h}=\frac{|d\tilde{\epsilon}^p(\phi)|}{|d\tilde{\sigma}|}. \tag{26}$$

Reciprocally, the plastic response can be expressed in terms of these quantities. Let us define the unitary vectors $\hat{\psi}$ and $\hat{\psi}^\perp$. The first one is oriented in the direction of ψ and the second one is the 90° rotation of $\hat{\psi}$. The plastic strain is written in this basis as

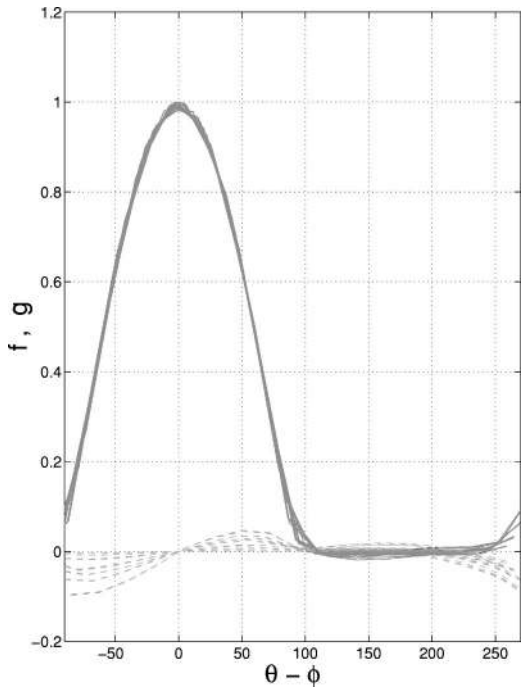

FIG. 13. Plastic profiles $f(\theta)$ (solid line) and $g(\theta)$ (dashed line). The results for different stress values have been superposed.

$$d\tilde{\epsilon}^p(\theta)=[(d\tilde{\epsilon}^p)^T\hat{\psi}]\hat{\psi}+[(d\tilde{\epsilon}^p)^T\hat{\psi}^\perp]\hat{\psi}^\perp$$

$$\equiv\frac{1}{h}[f(\theta)\hat{\psi}+g(\theta)\hat{\psi}^\perp]. \tag{27}$$

The plastic profiles $f(\theta)$ and $g(\theta)$ are shown in Fig. 13. The first one is approximately the same for all the stress states, and can be well fitted to a cosine function, centered on the yield direction ϕ and truncated to zero for the negative values. The last profile depends on the stress value, and is difficult to evaluate, because it is of the same order as the statistical fluctuations. However, the contribution of g to the total strain response is negligible. In order to simplify the description of the plastic response, the following approximation is made:

$$g(\theta)\ll f(\theta)\approx[[\cos(\theta-\phi)]]=[[\hat{\phi}^T\hat{\theta}]], \tag{28}$$

where $[[\cdot]]$ defines the function

$$[[x]]=\begin{cases}0, & x\leqslant 0,\\ x, & x>0.\end{cases} \tag{29}$$

Now, the flow rule results from the substitution of Eqs. (27) and (28) into Eq. (12),

$$J(\theta)d\tilde{\sigma}=\frac{[[\hat{\phi}^T d\tilde{\sigma}]]}{h}\hat{\psi}. \tag{30}$$

The yield direction and the flow direction have been calculated for different stress states. The results are shown in Fig. 14. Both angles are quite different, which is a clear deviation from Drucker's normality postulate [20]. Indeed,

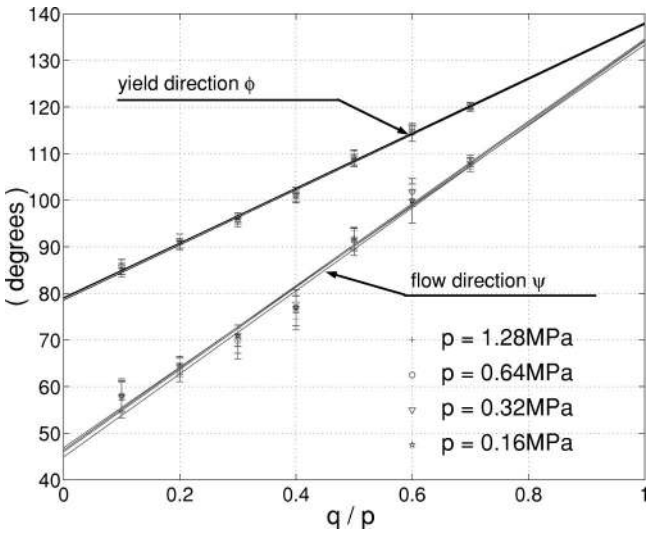

FIG. 14. The flow direction and the yield direction of the plastic response. Solid lines represent a linear fit.

many experimental results on soil deformation [21] have confirmed that these angles are completely different. Thus Drucker's postulate is not fulfilled in the deformation of granular materials, and the main reason for that is the rearrangement of contacts on small deformations, which are not taken into account in this theory. On the other hand, all the sliding, opening, and other micromechanical rearrangements can be well handled in the discrete element formulation, which is more adequate to describe the soil deformation.

The material constants are evaluated from the dependence of the plastic quantities on the stress: the yield direction and the flow direction can be roughly approximated by straight lines,

$$\phi=\phi_0+\phi_0'\frac{q}{p},$$

$$\psi=\psi_0+\psi_0'\frac{q}{p}. \tag{31}$$

The four material parameters $\phi_0=46^\circ\pm0.75^\circ$, $\phi_0'=88.3^\circ\pm0.6^\circ$, $\psi_0=78.9^\circ\pm0.2^\circ$, and $\psi_0'=59.1^\circ\pm0.4^\circ$ are obtained from the linear fit of the data. On the other hand, Fig. 15 shows that the plastic modulus depends on the stress through a power law relation,

$$h=h_0\left[1-\frac{q}{q_0}\left(\frac{p_0}{p}\right)^\vartheta\right]^\eta. \tag{32}$$

There are four additional material parameters: The plastic modulus $h_0=14.5\pm0.05$ at $q=0$, the constant $q_0=0.85\pm0.05$, and the exponents $\eta=2.7\pm0.04$ and $\vartheta=0.99\pm0.02$.

The plastic limit surface is given by the stress states where the plastic deformation becomes infinite. According to the flow rule [Eq. (30)], it is found, looking for the stress values, where Eq. (32) vanishes,

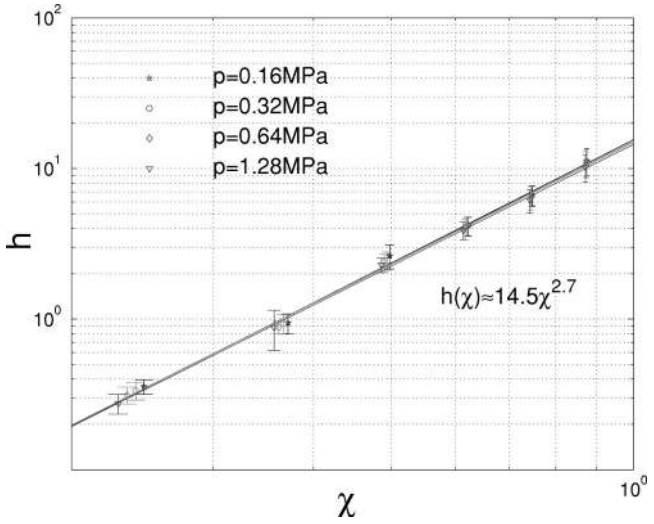

FIG. 15. Plastic modulus. The solid line is a power law fit with respect to the variable $\chi = 1 - (p/p_0)^{\vartheta} q/q_0$.

$$\frac{q_p}{q_0} = \left(\frac{p}{p_0}\right)^{\vartheta}. \tag{33}$$

It is important to point out that the failure surface—given in Eq. (13)—does not correspond to the plastic limit surface. Actually, this matter has already been discussed in the framework of Hill's condition of instability [22] the bifurcation analysis [23], which predicts that the instability should be reached strictly inside the plastic limit surface.

V. CONCLUDING REMARKS

The elastoplastic response of a Voronoi tessellated sample of polygons has been calculated in the case of monotonic and quasistatic loading. It can be written in a simple form as

$$d\tilde{\epsilon} = D(d)d\tilde{\sigma} + \frac{[[\hat{\phi}^T d\tilde{\sigma}]]}{h}\hat{\psi}. \tag{34}$$

The plastic response reflects the nonassociated features of realistic soils. Here the yield direction and flow direction are linearly related to the ratio q/p, and the plastic modulus obeys a power law relation with a weak pressure dependence. The classical parameters of elasticity—Young's modulus and Poisson's ratio—are not material constants, because they depend on the internal damage parameter. Therefore, Eq. (34) is not complete, and it is necessary to include the relation between the internal damage and the external load. By focusing on the details of the dynamics of the microcontacts, a significant progress may be made in the investigation of the continuous models.

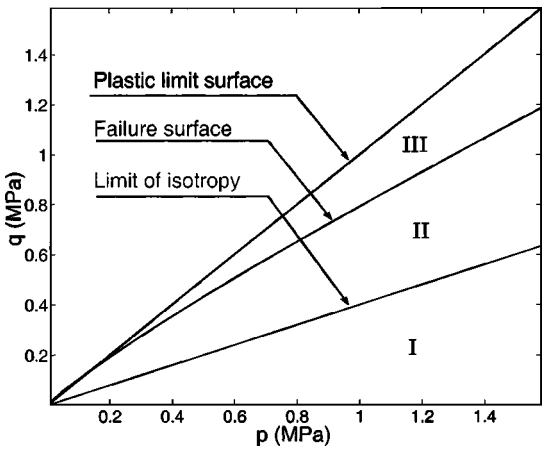

FIG. 16. Elastoplastic regimes: isotropic (I), anisotropic (II), and unstable (III).

The elastoplastic response leads to the identification of three different regimes which are shown in Fig. 16. Zone I corresponds to the isotropic regime, characterized by small plastic deformations and a linear elastic regime. In zone II open contacts are detected, which must be taken into account in the calculation of the nonlinear elasticity. Zone III corresponds to unstable states so that the stress-strain relation cannot be calculated here. The extrapolation of the strain response in this region shows that the plastic strain must have a finite value just before the instability is reached.

The above observation leads to the open question of the nature of the failure [22]. Numerical simulations on strain controlled tests show that strain localization is the most typical mode of failure. The fact that it appears before the sample reaches the plastic limit surface suggests that the appearance of the instability is not completely determined by the macroscopic state.

The role of the microstructure on the strain localization has been intensely studied in the last years [23,24]. Future work is the creation of samples with different granular textures—for example, changing the void ratio distributions and the polydispersity of the grains. Then we can deal with the question that how does a change in the microstructure affect the elastoplastic response and the strain localization.

ACKNOWLEDGMENTS

We thank F. Darve, P. Vermeer, F. Kun, J. Åstrøm, and S. Luding for helpful discussions and acknowledge the support of the Deutsche Forschungsgemeinschaft within the research group Modellierung kohäsiver Reibungsmaterialen.

[1] P.A. Vermeer, in *Constitutive Relations of Soils*, edited by G. Gudehus, F. Darve, and L. Vardoulakis (Balkema, Rotterdam, 1984), pp. 175–197.
[2] D. Kolymbas, Arch. Appl. Mech. **61**, 143 (1991).
[3] P.A. Cundall, Ingenievr Archiv. **59**, 769 (1989).
[4] F. Radjai, M. Jean, J.J. Moreau, and S. Roux, Phys. Rev. Lett. **77**, 274 (1996).
[5] C. Thornton, Acta Mech. **64**, 45 (1986).

[6] H. Tillemans and H.J. Herrmann, Physica A **217**, 261 (1995).
[7] F. Kun and H.J. Herrmann, Comput. Methods Appl. Mech. Eng. **138**, 3 (1996).
[8] F. Kun and H.J. Herrmann, Int. J. Mod. Phys. C **7**, 837 (1996).
[9] F. Kun and H.J. Herrmann, Phys. Rev. E **59**, 2623 (1999).
[10] L. Brendel and S. Dippel, in *Proceedings of Physics of Dry Granular Media*, Vol. 350, *NATO Advanced Studies Institute*, *Series E: Applied Sciences*, edited by H.J. Herrmann, J.-P. Hovi, and S. Luding (Kluwer Academic, Dordrecht, 1998), pp. 313–318.
[11] J.A. Åstrøm,, H.J. Herrmann, and J. Timonen, Phys. Rev. Lett. **84**, 638 (2000).
[12] S. Luding, in *Proceedings of Physics of Dry Granular Media* (Ref. [10]), pp. 285–304.
[13] N.P. Kruyt and L. Rothenburg, ASME J. Appl. Mech. **118**, 706 (1996).
[14] L. Oger, S.B. Savage, D. Corriveau, and M. Sayed, in *Powders & Grains 97*, edited by R.P. Behringer and J.T. Jenkins (Balkema, Rotterdam, 1997), pp. 283–286.
[15] F. Darve, in *Geomaterials Constitutive Equations and Modeling*, edited by F. Darve (Elsevier Science, London, 1990), pp. 123–148.
[16] J.P. Bardet, Int. J. Plast. **10**, 879 (1994).
[17] N.G.W. Cook and K. Hodgson, J. Geophys. Res. **70**, 2883 (1965).
[18] M. Lätzel, S. Luding, and H.J. Herrmann, Granular Matter **2**, 123 (2000).
[19] M. Oda, J. Konishi, and S. Nemat-Nasser, Mech. Mater. **1**, 267 (1982).
[20] D.C. Drucker and W. Prager, Q. Appl. Math. **10**, 157 (1952).
[21] F. Tatsuoka and K. Ishihara, Soils Found. **14**, 63 (1974).
[22] F. Darve and F. Laouafa, Mech. Cohesive-Frict. Mater. **5**, 627 (2000).
[23] I. Vardoulakis, Int. J. Numer. Analyt. Meth. Geomech. **4**, 113 (1980).
[24] G. Viggiani, M. Küntz, and J. Desrues, Lect. Notes Phys. **568**, 111 (2001).